Magnetoshell Aerocapture: Advances Toward Concept Feasibility

Charles L. Kelly

A thesis
submitted in partial fulfillment of the
requirements for the degree of

Master of Science in Aeronautics & Astronautics

University of Washington

2018

Committee:

Uri Shumlak, Chair

Justin Little

Program Authorized to Offer Degree:
Aeronautics & Astronautics

University of Washington

Abstract

Magnetoshell Aerocapture: Advances Toward Concept Feasibility

Charles L. Kelly

Chair of the Supervisory Committee:
Professor Uri Shumlak
Aeronautics & Astronautics

Magnetoshell Aerocapture (MAC) is a novel technology that proposes to use drag on a dipole plasma in planetary atmospheres as an orbit insertion technique. It aims to augment the benefits of traditional aerocapture by trapping particles over a much larger area than physical structures can reach. This enables aerocapture at higher altitudes, greatly reducing the heat load and dynamic pressure on spacecraft surfaces. The technology is in its early stages of development, and has yet to demonstrate feasibility in an orbit-representative environment. The lack of a proof-of-concept stems mainly from the unavailability of large-scale, high-velocity test facilities that can accurately simulate the aerocapture environment. In this thesis, several avenues are identified that can bring MAC closer to a successful demonstration of concept feasibility.

A custom orbit code that dynamically couples magnetoshell physics with trajectory propagation is developed and benchmarked. The code is used to simulate MAC maneuvers for a 60 ton payload at Mars and a 1 ton payload at Neptune, both proposed NASA missions that are not possible with modern flight-ready technology. In both simulations, MAC successfully completes the maneuver and is shown to produce low dynamic pressures and continuously-variable drag characteristics. A generalized magnetoshell design framework is described for application to satellites of any scale. This framework is applied to develop a flight demonstration mission aboard a 3U CubeSat with a deployable electromagnet. The

CubeSat configuration considered here proves to be intractable due to limitations on stored energy, mass, and deployment scheme. As an alternative to a flight demonstration, a laboratory proof-of-concept is proposed as a subscale magnetoshell interacting with a neutral particle flow in an experimental setting. The suitability of neutral beams used in silicon etching is considered for use as a flow source. An experimental design is proposed using such a source. Investigative techniques are considered that aim to characterize the power and fuel requirements of the plasma as well as the structure of the flow ionization region. This experiment can resolve the difficulties of both full-scale ground testing and in-orbit demonstration.

The work in this thesis advances MAC closer to realization in interplanetary missions, enabling experimentalists and mission planners to further develop the technology. By addressing some of the biggest impediments to successful demonstration, this thesis helps to push MAC toward competitiveness with other proposed aerocapture solutions.

TABLE OF CONTENTS

Page

List of Figures iii

List of Tables iv

Chapter 1: Introduction 1
1.1 Modern Orbit Insertion 1
1.2 Magnetoshell Aerocapture 5
1.3 Motivation for This Thesis 9

Chapter 2: Background 11
2.1 Magnetoshell Physics 11
2.2 Parameter Scaling 13
2.3 State of the Art 16
2.4 Summary 18

Chapter 3: Orbit Model 19
3.1 Equation of Motion 19
3.2 Model Benchmarking 20
3.3 Continuously-Variable Drag 22
3.4 Mission Simulations 23
3.5 Discussion 25

Chapter 4: CubeSat Demonstration Mission 27
4.1 System Design 27
4.2 CubeSat Mission 31
4.3 Discussion 34

Chapter 5: Subscale Experiment Design 37
5.1 Low-Energy Neutral Beams 37
5.2 Experiment Design 40
5.3 Discussion 43

Chapter 6: Conclusion 45

Bibliography 47

LIST OF FIGURES

Figure Number		Page
1.1	Diagram of an aerocapture maneuver [5].	3
1.2	Comparison of payload delivery costs for aerocapture and non-aerocapture orbit insertion mission architectures [3].	4
1.3	Artist's depiction of a magnetoshell operating in Mars' atmosphere [14].	6
1.4	Representative comparison of a small-satellite orbit injection using a regular heat shield versus a larger magnetoshell. The higher altitude MAC maneuver dramatically reduces the dynamic pressure while achieving the same drag and Δv.	8
2.1	Cross-section view of the magnetoshell interaction with neutral atmosphere in a frame moving with the spacecraft.	12
2.2	RMF magnetoshell tech demo. The magnetoshell is near the center while the MPD thruster plume is seen at top [14].	16
2.3	Mock 6U CubeSat with RF plasma injection at its center operating with Argon at 200 sccm, 300 W RF power, and $B_0 = 0$ Gauss (left) and 172 Gauss (right) [20].	17
3.1	Comparison of simulations of a Martian aerocapture maneuver with Copernicus and a custom Mathematica code.	21
3.2	MAC for a 1 ton Neptune payload (left) and 60 ton Mars payload (right).	25
4.1	Burn time optimization.	32
4.2	Internal CubeSat notional hardware.	33
4.3	Magnet-stowed and magnet-deployed configurations of the CubeSat.	34
4.4	Mission profile for the MAC CubeSat. The magnetoshell is activated for 800 s every two days until deorbit.	35
5.1	Diagram of an ICP neutral beam source using an ion extraction and neutralization grid [38].	38
5.2	Effect of plasma moulding on the surface neutralization of ions [37].	39
5.3	Possible layout for subscale magnetoshell ground test with ICP neutral beam.	41

LIST OF TABLES

Table Number Page

1.1 Comparison of payload mass delivered for aerocapture and non-aerocapture orbit insertion mission architectures (adapted from [3]). 5

3.1 Assumptions (top half) and some key results (bottom half) for Neptune and Mars mission simulations using MAC. 24

4.1 CubeSat system-level design parameters. 32

5.1 Design parameters for a potential subscale magnetoshell experiment. The top section details the magnetoshell while the bottom section details the ICP neutral beam. 42

Chapter 1
INTRODUCTION

1.1 Modern Orbit Insertion

One of the biggest challenges to exploring the solar system with satellites is that of orbit insertion. Interplanetary spacecraft approach their targets along hyperbolic trajectories, often with large excess velocity. A change in velocity (Δv) must be imparted to reduce the spacecraft's energy and put it in a closed orbit around the target body; otherwise, the mission is a fly-by and can only collect science for the short duration of its encounter with the target. Orbiting spacecraft are much preferred to fly-bys as the science return is much higher.

Every interplanetary orbiter to date has achieved this Δv using chemical propulsion. This is problematic, as the rocket equation demands an exponential increase in fuel mass for linearly increasing Δv. Mission planners circumvent this problem by reducing the approach velocity and conserving as much fuel mass as possible before target arrival. For instance, the Cassini orbiter was able to capture at Saturn with a Δv of only 613 m/s, but getting there with enough fuel to perform this burn took seven years and four gravity assists at three different planets [1]. A trajectory of such complexity severely limits launch windows and mission lifetime. Additionally, no spacecraft has ever orbited Neptune or Uranus because chemical propulsion cannot deliver enough mass for a meaningful science mission. For example, a mission to Neptune that minimizes insertion Δv would take 30 years to arrive, while a shorter trajectory demands an impossibly high Δv of 7 km/s [2]. Instead, these gas giants have only been observed in-situ once each, during the brief fly-bys of Voyager 2 in the 1980s.

For these types of missions, alternatives to chemical rockets must be examined. Electric

propulsion (EP) appears attractive for its high specific impulse and therefore low fuel consumption. However, these devices struggle to produce enough thrust to shed the hyperbolic orbital energy in the short duration of an orbit insertion window. Additionally, modern EP is powered by solar energy; though it could one day work for orbit insertion at Mars and Venus [3], the solar flux is simply too small at outer planets to be harvested for high thrust [4]. It is clear that the disadvantages of propulsive orbit insertion are a leading cause of limitations to our ability to orbit solar system bodies.

One solution to the drawbacks of propulsion is the use of aerocapture. Instead of using thrust to achieve the Δv required for capture into a stable orbit, this maneuver uses the aerodynamic drag force of the target body's atmosphere on the spacecraft. A typical aerocapture maneuver is shown in Figure 1.1. The spacecraft enters the atmosphere along its hyperbolic trajectory and leaves the atmosphere on an elliptical orbit. The perigee of this orbit still resides inside the atmosphere, so a small correction burn is performed at apogee to ensure the spacecraft does not deorbit on subsequent passes. Aerocapture is part of a broader class of orbit maneuvers known as aeroassists in which atmospheric drag is used to effect a change in the spacecraft's trajectory. The distinguishing characteristic of aerocapture among other aeroassist maneuvers is the transition from hyperbolic to closed orbit in a single pass through the atmosphere.

Aerocapture offers significant benefits over traditional propulsive orbit insertion. Hall et al. [3] demonstrate a large advantage in both cost and delivered mass for missions to all eight solar system desinations with tangible atmospheres (see Figure 1.2 and Table 1.1). Additionally, they identify aerocapture as an enabling technology for otherwise infeasible missions to Jupiter, Saturn, and Neptune. Several proposed mission architectures have called for the use of aerocapture, such as a Venus low-circular orbiting probe [6], a Cassini-style orbiter/lander mission at Titan [7], crew return to Earth [8], and the Human Mars DRA 5.0 [9], among others.

The primary aim of aerocapture devices is to lower the ballistic coefficient β of the reentry

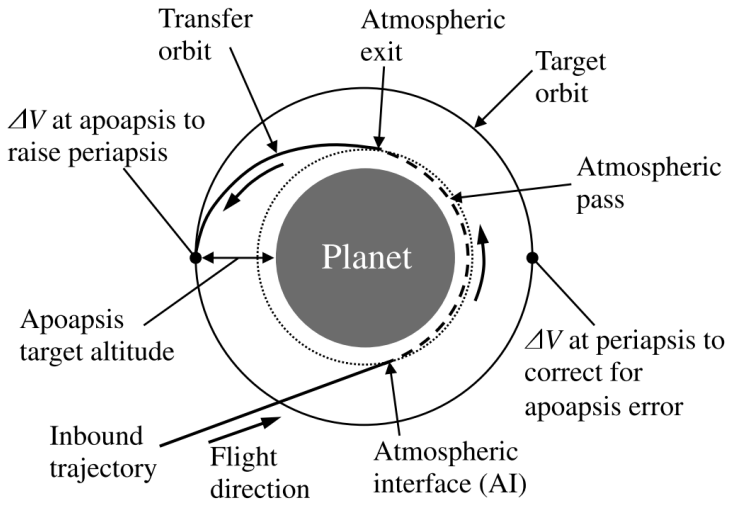

Figure 1.1: Diagram of an aerocapture maneuver [5].

vehicle, where

$$\beta = \frac{m}{C_D A} \tag{1.1}$$

is the ratio of vehicle mass m to drag coefficient C_D times cross-sectional area A. β represents a ratio between inertial and drag forces; lowering β enhances the effect of drag on reducing orbital energy. In practice, this amounts to developing systems with larger drag areas than a typical reentry heat shield offers. The drag force on the spacecraft and aerocapture device is given by

$$F_D = \frac{1}{2}\rho v^2 C_D A \tag{1.2}$$

where F_D is drag force, ρ is atmospheric density, and v is spacecraft speed. Equation (1.2) indicates that for a constant spacecraft mass, decreasing β results in higher drag.

Some relatively mature aerocapture and planetary entry technologies exist that all focus on drastically increasing the drag area of the reentry vehicle. The Hypersonic Inflatable Aerodynamic Decelerator (HIAD) uses a series of concentric inflatable rings to create a large, lightweight shell extending beyond the diameter of the spacecraft. HIAD has been studied and ground-tested extensively up to deployed diameters of around 6 meters [10]. Additionally,

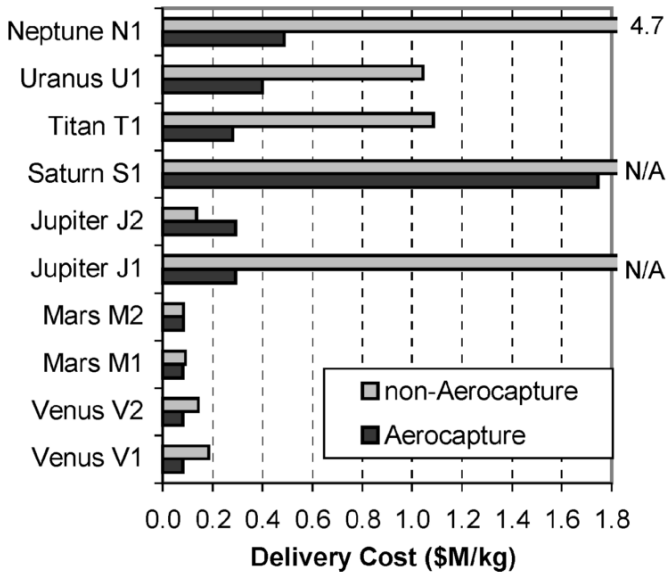

Figure 1.2: Comparison of payload delivery costs for aerocapture and non-aerocapture orbit insertion mission architectures [3].

it has successfully demonstrated deployment of a 3 meter-diameter cone in suborbital flight tests [11]. The Adaptive Deployable Placement Technology (ADEPT) extends a similarly-sized rigid structure acting as an aeroshell for the spacecraft [12]. Yet another concept aims to use "ballutes" (balloon parachute) to generate drag on large inflated surfaces either clamped to the spacecraft or towed behind it [13].

Despite the clear advantages of aerocapture for orbit insertion, none of these concepts has ever been used on a mission because of the associated risks. According to Equation (1.2), drag force increases with atmospheric density. This means that successful aerocapture relies on plunging deep into the atmosphere to achieve the extroordinary drag it requires. Since the aforementioned technologies are of a similar diameter to the spacecraft itself, taking such a low-altitude trajectory at hyperbolic insertion speeds still requires complex and heavy thermal protection to guard the craft from extreme heat and dynamic pressure. Furthermore, these static devices offer little or no control of their drag surfaces during flight, leaving the vehicle vulnerable to local density disturbances.

Mission	Best A/C mass, kg	Best non-A/C mass, kg	% Increase
Venus V1	5078	2834	79
Venus V2	5078	3542	43
Mars M1	5232	4556	15
Mars M2	5232	4983	5
Jupiter J1	2262	< 0	Infinite
Jupiter J2	2262	4628	-51
Saturn S1	494	< 0	Infinite
Titan T1	2630	691	280
Uranus U1	1966	618	218
Neptune N1	1680	180	832

Table 1.1: Comparison of payload mass delivered for aerocapture and non-aerocapture orbit insertion mission architectures (adapted from [3]).

1.2 Magnetoshell Aerocapture

The risks detailed above unfortunately leave aerocapture tantalizingly out of reach for mission planners. Such a barrier highlights the need for a feasibility breakthrough in aerocapture technology. One novel concept aims to replace traditional hard-body decelerators with a magnetic dipole plasma called a magnetoshell. This device captures atmospheric particles and imparts their momentum to the spacecraft, acting like a "plasma parachute" to generate a drag force. Whereas modern aeroshells deflect the atmospheric flow, Magnetoshell Aerocapture (MAC) uses a plasma interaction to ionize atmospheric neutral particles and temporarily confine them in the magnetic field. It seeds a small amount of plasma in the dipole from onboard propellant and the ionized atmosphere fuels it otherwise. A concept image of a magnetoshell operating in the Martian atmosphere is shown in Figure 1.3.

MAC is similar in concept to magnetic sails proposed for interplanetary space propulsion, such as M2P2 by Winglee et al. [15] or the plasma magnetosphere by Slough [16]. These

Figure 1.3: Artist's depiction of a magnetoshell operating in Mars' atmosphere [14].

operate by inflating a very large (10–100 km scale) dipole magnetic field that both deflects and captures high-energy particles from the solar wind. The device size and the energy in the solar plasma work together to produce a thrust force capable of accelerating spacecraft to tens of kilometers per second. Critical to both MAC and magnetic sails is the use of a dipole magnetic field to enhance the effective area over which in-situ particles push on the spacecraft. However, a few important characteristics distinguish MAC from magnetic sails. First, the required braking force for aerocapture is much higher than the expected capability of the magnetic sail concepts (much like the drawback of EP for orbit insertion). Second, MAC takes advantage of a significantly higher-density flow (planetary atmosphere versus solar wind), thereby dictating a much smaller scale size due to the large energy requirements associated with confining so many particles. Despite their physical similarities, it is evident that magnetic sails are ill-suited for orbit insertion, much as MAC is inadequate for in-space propulsion.

1.2.1 Advantages of Magnetoshell Aerocapture

The primary benefit motivating MAC as a game-changing orbit insertion tool is the reduction of atmospheric heating and pressure on the spacecraft. The extent of plasma confinement, which determines the effective drag area, can be made sufficiently large by controlling power application to the magnet. This can result in a drag diameter significantly larger (∼10–100 m) than the spacecraft or any modern aeroshell (∼1–10 m). The larger area allows MAC to operate at lower atmospheric density without compromising drag force per Equation (1.2). Dynamic pressure,

$$Q = \frac{1}{2}\rho v^2, \tag{1.3}$$

is a measure of kinetic energy in the flow impacting the spacecraft and dictates the wall heat flux due to flow stagnation against the vehicle. Q depends on density but not area; therefore, performing aerocapture with larger area and lower density maintains the same drag force while distributing the heat and pressure loads over a larger surface. Figure 1.4 offers a comparison of the drag and dynamic pressure forces between a traditional aeroshell and a magnetoshell. Since MAC potentially offers orders-of-magnitude larger drag area than modern aeroshells, it takes a large step toward eliminating the current hurdles restricting aerocapture.

Another unique feature of MAC is the ability to modulate the drag area through control of the magnetic field strength. Such modulation is a control variable that may be leveraged to make aerocapture more robust to variations in the target atmosphere. Robustness is crucial for interplanetary craft, as empirical atmospheric data on outer planets and moons is relatively scarce. For existing drag-only aerocapture devices (like the ballute), the only form of drag modulation is to jettison the device. The spacecraft monitors the projected trajectory during the maneuver and releases the device once its projection matches the target orbit. The sensitivity of this technique to atmospheric density and flight path uncertainties has been investigated. Works by Putnam et al. [17] and Westhelle et al. [18] both found that the sensitivity depends largely on the ratio of ballistic coefficients before (β_1) and after (β_2)

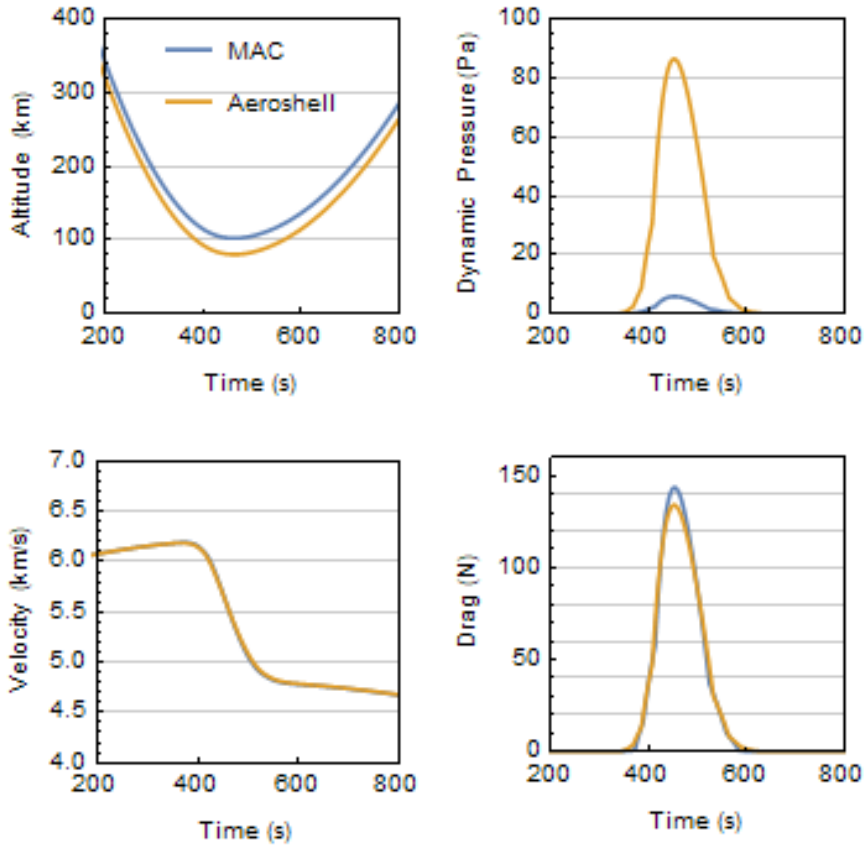

Figure 1.4: Representative comparison of a small-satellite orbit injection using a regular heat shield versus a larger magnetoshell. The higher altitude MAC maneuver dramatically reduces the dynamic pressure while achieving the same drag and Δv.

the jettison event. Increasing β_2/β_1 (in other words, increasing the aerocapture device area relative to spacecraft-only area) resulted in significant improvement to the flight corridor.[1] These results indicate that, even without active modulation, MAC has the potential for highly robust maneuvers due to its large area compared to the spacecraft.

Later work by Putnam and Braun [5] investigated the sensitivity of continuously-variable (CV) drag modulation for aerocapture. A CV aerocapture system is one that can change

[1]The flight corridor in this case describes the set of velocities and flight path angles at atmospheric entry for which the target orbit can be attained. Improving the corridor means that the strict requirements on flight conditions entering the atmosphere can be relaxed.

its drag area as necessary along the flight path in order to tightly control the projected trajectory; therefore, MAC falls into the CV device category. The β-ratio for a CV device is defined as the ratio of the spacecraft-only β to the minimum β achievable by the modulated device. Putnam and Braun found that the acceptable flight corridor depends exclusively on the β-ratio for both CV and single-jettison systems. Furthermore, they found that a CV system with the same β-ratio as the single-jettison device is capable of better apoapsis-targeting accuracy and lower Δv required for the post-aerocapture correction burns.[2] The results of these works on flight sensitivities indicate that a low-β, CV device such as MAC will offer superior orbit-targeting capability compared to modern aeroshells.

1.3 Motivation for This Thesis

Though MAC promises to solve many of the problems to aerocapture, the concept remains low-TRL.[3] One of the primary reasons is the difficulty of ground-testing a device that is inherently large-scale in a low density, high velocity regime simulating hyperbolic reentry. There are no modern wind tunnels possessing the needed characteristics for a full-scale MAC proof-of-concept. Therefore, the concept must be proven either by performing a flight demonstration aboard a satellite or by developing novel experimental approaches. A flight demonstration requires careful analysis utilizing plasma-based trajectory modelling, while a wind tunnel test demands development of special flow generators and diagnostics. In this work, MAC is advanced toward such a proof-of-concept. Demonstration of this technology's feasibility and characterization of performance and scaling are necessary for it to be considered by designers of interplanetary mission architectures. By directing the body of research toward successful demonstration, this thesis intends to bring MAC closer to mid-TRL and open up its use to researchers and mission planners.

---

[2]See Figure 1.1 for reference.

[3]Technology Readiness Level (TRL) is a scale used by NASA to define a space technology's state of development.

1.3.1 Organization

Chapter 2 will expand upon the physics of magnetoshell interaction with the atmosphere and experimental work previously conducted on MAC. Chapter 3 details the development of an orbit trajectory code that employs some of these physics to generate realistic flight paths. Chapter 4 lays the groundwork on a parameter design space for using MAC aboard satellites and describes a potential CubeSat flight demonstration mission. Chapter 5 discusses a possible design for an experiment testing MAC feasibility. Chapter 6 summarizes the findings and recommendations presented throughout the work and discusses potential future work.

Chapter 2
BACKGROUND

2.1 Magnetoshell Physics

The magnetoshell generates drag by interacting with the flow rather than deflecting it like typical aeroshells. The primary interaction is resonant charge exchange between plasma ions and atmospheric neutrals, which has the form

$$X^+ + X \rightarrow X + X^+ \tag{2.1}$$

for species X. To see how this process induces drag, the interaction is observed in a frame moving with the magnetoshell such that the plasma is stationary and neutrals stream in unidirectionally at a speed equal to the spacecraft's orbital velocity v. See Figure 2.1 for a simple diagrammatic picture. The magnetoshell uses its magnetic field to contain a spherical or toroidal region of plasma. A neutral particle with a large directional kinetic energy encounters this plasma. It undergoes charge exchange with an ion having some small, randomly directed energy. Because charge exchange conserves particle energy, this thermal ion becomes a thermal neutral and diffuses out of the system, no longer confined by magnetic forces. The original neutral, however, becomes a high-energy ion that is turned by the magnetic field through the Lorentz force. This turning is responsible for imparting the momentum of the particle to the magnet and, subsequently, to the spacecraft itself. Though each individual particle produces a miniscule force, the charge exchange reaction is so widespread that large macroscopic drag can occur. The aggregate effect is that the magnetoshell appears impenetrable to atmospheric neutrals out to a diameter several times the size of the magnet.

One critical aspect of the magnetoshell used for MAC is that it is a low-β_p configuration.

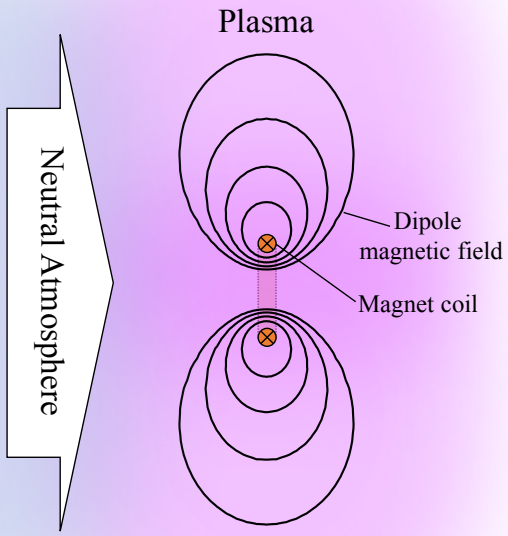

Figure 2.1: Cross-section view of the magnetoshell interaction with neutral atmosphere in a frame moving with the spacecraft.

Not to be confused with the ballistic coefficient β from Equation (1.1), β_p is the ratio of plasma pressure to magnetic pressure:

$$\beta_p = \frac{p}{B^2/2\mu_0} \tag{2.2}$$

where p is plasma pressure, B is magnetic field strength, and μ_0 is vacuum permeability. A dipole plasma can operate in both high- and low-β_p configurations. Having high β_p would be advantageous for enhancing the charge exchange reaction rate, but sustaining such a plasma is extremely energy intensive. For example, the Levitated Dipole Experiment required super-

conducting magnets to achieve a peak β_p of 20% [19]. Employing superconductors aboard a spacecraft would entail structural, cryogenic, and power system complexities rendering MAC inferior to its rigid counterparts. Instead, the magnetoshell sustains $\beta_p < 1\%$ using only a resistive electromagnet. The advantages to this configuration are twofold. First, it substantially reduces the engineering complexity of the device. Second, low-β_p means the magnetic field profile is not susceptible to the rapid plasma fluctuations potentially occurring during the aerocapture maneuver. This allows models to assume the plasma density follows the magnetic field strength closely, easing analytic and computational analysis. This also means the device can be reliably modulated just through its magnetic field strength.

2.2 Parameter Scaling

Kirtley has developed an analytic model of the magnetoshell that is useful for relating plasma and magnet parameters to expected performance [14]. Section 2.2 is a summary of the model. Though these relations provide only a first-order picture of magnetoshell scaling, they are useful for understanding the basic regimes of MAC.

The magnetoshell is considered to be a cylinder of arbitrary length and axisymmetry with neutrals flowing into it end-on. The magnetic field profile $B(r)$ is taken to be the vacuum case for a dipole with a constant field strength in the center of the magnet:

$$B(r) = \begin{cases} B_0, & r \leq R_m \\ B_0 \left(\frac{R_m}{r}\right)^3, & r > R_m \end{cases} \tag{2.3}$$

where B_0 is the center-field strength and R_m is the magnet coil radius. The plasma density $n(r)$ follows the same profile due to low β_p:

$$n_i(r) = n_e(r) = \begin{cases} n_0, & r \leq R_m \\ n_0 \left(\frac{R_m}{r}\right)^3, & r > R_m \end{cases} \tag{2.4}$$

where n_0 is the center-field density and quasineutrality is assumed.

2.2.1 Magnetoshell Size

Drag is modelled as though the magnetoshell is a solid object of effective cross-sectional area A_e using equation (1.2). To determine A_e, single particle dynamics are considered. A newly-ionized particle in the magnetoshell (resulting from charge exchange of a neutral) has a Larmor radius

$$r_i = \frac{m_i v}{qB} \tag{2.5}$$

that depends on its mass m_i, charge q, velocity v, and the magnetic field B where it is generated. Recall that its velocity is equal to the orbital speed since particle energy is conserved in the charge exchange reaction. This ion is considered "trapped" if r_i is smaller than the characteristic size L_0 of the magnetoshell:

$$\frac{r_i}{L_0} = \frac{m_i v}{qBL_0} < 1. \tag{2.6}$$

Recalling that B is a function of r, the effective trapping radius R_e is found by solving $r_i|_{r=R_e} = R_e$:

$$R_e^2 = \frac{R_m^3}{r_{i,0}} = A_e/\pi \tag{2.7}$$

where $r_{i,0} = \frac{m_i v}{qB_0}$ is the center-field ion Larmor radius. Equation (2.7) dictates the effective area of the cylindrical geometry, $A_e = \pi R_e^2$.

2.2.2 Density Limitations

The trapping area A_e is well-defined to first order by equation (2.7). However, this treatment so far has not considered particle collisions. Collisions will dictate many bulk processes in the magnetoshell like diffusion, thermalization, ionization, and more, but these are ignored for now in favor of the single-particles treatment as before.

To ensure the new ion transfers momentum to the magnet, it must not undergo secondary collisions before completing an orbit. In practical terms, this means the ion Hall parameter Ω_i should be greater than unity,

$$\Omega_i = \frac{\omega_{c,i}}{\nu_i} > 1, \tag{2.8}$$

where $\omega_{c,i}$ is the ion cyclotron frequency and ν_i is the ion collision frequency. Only charge exchange ion collisions are considered since these neutralizing interactions will cause the particle to leave the system before transferring its momentum. The constraint from Equation (2.8) can be rewritten in a form that introduces atmospheric density. $\Omega_i > 1$ implies that the mean free path for charge exchange λ_{cx} is greater than the distance traveled by the ion in a Larmor orbit:

$$\lambda_{cx} = \frac{1}{n_n \sigma_{cx}} > \pi r_i \tag{2.9}$$

where n_n is the neutral species density and σ_{cx} is the cross section for charge exchange. The dependence of constraint (2.9) on n_n indicates an upper bound on atmospheric density $\rho \sim n_n$ for effective drag production. At high density, λ_{cx} can become so short that Equation (2.9) is not satisfied anywhere inside the trapping radius R_e. In other words, the neutral density is so high that the magnetoshell ions are too collisional to become trapped as described in Section 2.2.1. This limits the altitude of operation for MAC since a maneuver too low in the atmosphere will not be able to effectively generate drag.

There must also be a high likelihood of charge exchange reactions to produce significant drag. In other words, the plasma must be relatively impenetrable to neutrals for us approximate drag as Equation (1.2). The charge exchange mean free path must then be shorter than the scale length of the plasma:

$$\lambda_{cx} = \frac{1}{n_n \sigma_{cx}} < L_0. \tag{2.10}$$

Constraint (2.10) implies some minimum neutral density required to generate drag. Note that Equation (2.9) has a spatial dependence through $r_i(r) \propto r^3$ whereas Equation (2.10) depends only on the macroscopic scale of the magnetoshell $L_0 \propto R_e$.

Together, Constraints (2.9) and (2.10) draw a region of atmospheric densities, and therefore altitudes, over which MAC can effectively operate. Equations (1.2) and (2.7) describe how the drag force scales in this operational regime. In this way, Kirtley's model can be used for first-order designs of spacecraft at the system level, flight trajectories, and experimental apparatus.

Figure 2.2: RMF magnetoshell tech demo. The magnetoshell is near the center while the MPD thruster plume is seen at top [14].

2.3 State of the Art

2.3.1 Experimental Investigation

Despite the difficulty of accurately ground-testing MAC, some experimental efforts have been made. Kirtley developed a small magnetoshell technology demonstration [14] using a rotating-magnetic-field (RMF) ionization scheme and a small (∼10 cm-diameter) dipole magnet (see Figure 2.2). The magnetoshell was mounted on a dielectric post extended from a torsional thrust stand to measure drag. The flow impinging on the magnetoshell was formed by a pulsed miniature MPD thruster purpose-built for the tech demo. The drag force was measured from the thrust stand in both magnet-on and magnet-off conditions so as to compare the effect of the plasma. Operating with $B_0 = 200$ Gauss and $A_e = 2.3$ m^2, 220 mN of drag was observed, a factor of 1,000 higher than the drag when deactivated. It must be noted that the MPD flow was ionized and had a velocity of only ∼1.7 km/s. Additionally, the densities of the impinging neutrals and magnetoshell plasma were not measured, so the contribution of charge exchange reactions to drag is unclear.

Figure 2.3: Mock 6U CubeSat with RF plasma injection at its center operating with Argon at 200 sccm, 300 W RF power, and $B_0 = 0$ Gauss (left) and 172 Gauss (right) [20].

Another technology demonstration by Kirtley [20] tested a notional onboard RF plasma injection scheme for a small satellite utilizing MAC. A mock 6U CubeSat was built with the dipole magnet wound around the 30×20 cm perimeter. It was shown that the magnetic field acts to populate the magnetoshell with the source plasma out to large diameters (see Figure 2.3). This result indicates that a seed plasma can be supplied by the spacecraft to ignite the magnetoshell at the start of MAC maneuvers.

2.3.2 Mission Studies

Kirtley has performed some system-level designs [14] of magnetoshells for missions that may benefit from the use of MAC. He analyzed feasibility of MAC for a Human Mars mission, specifically the Design Reference Architecture (DRA) 5.0 [9]. The 20 metric ton (Ton) aeroshell used by DRA 5.0 for cargo delivery can be replaced by a 1 Ton, 1400 m^2 magnetoshell to successfully deliver a 60 Ton payload to Mars orbit. This replacement leads to a reduction in initial mass in Low Earth Orbit of 80 Tons and consequently ∼$2 billion saved in launch costs. He also analyzed a Nepune orbiter architecture [21], a mission that is infeasible without aerocapture. It was found that MAC is capable of delivering 75% more mass to the planet than traditional aeroshells by deploying a 250 m^2 magnetoshell.

2.4 Summary

Magnetoshell drag is the result of leveraging resonant charge exchange to ionize planetary neutrals and trap them in a strong magnetic field. Parameters of importance are the magnetic field strength, magnet size, atmospheric density, and charge exchange cross-section, among others. Nearly all of the experimental work and theory development behind this understanding comes from Kirtley. His works provide a useful analytical framework for generating first-order performance expectations. The next chapter will show how such a model can be used to develop novel simulation tools.

Chapter 3
ORBIT MODEL

This chapter will detail a trajectory simulator that employs the magnetoshell drag model described in Section 2.2. A custom tool such as this is useful for analyzing MAC missions with higher fidelity than existing orbit propagators can provide. The unique physics of the magnetoshell must be treated correctly in the spacecraft drag model. An orbit code capturing magnetoshell physics is essential to determining plasma, magnet, and power parameters for a desired MAC maneuver (and vice versa).

3.1 Equation of Motion

A set of proper assumptions and equations to propagate the trajectory must be developed. For most aerocapture analyses, the maneuver timescale is short and by definition takes place in one pass.[1] Therefore, typical orbit perturbations due to body oblateness and third-body gravity can be ignored and a pointmass two-body gravity model is appropriate. Under these assumptions, the equation of motion is

$$\frac{d\vec{v}}{dt} = -\frac{\mu}{|\vec{r}|^3}\vec{r} - \frac{F_D}{m}\frac{\vec{v}}{|\vec{v}|} \tag{3.1}$$

where $\vec{r}$ and $\vec{v}$ are spacecraft position and velocity respectively, m is spacecraft mass, μ is the gravitational parameter of the target body, and F_D is drag force on the craft.

The drag is modelled as Equation (1.2) incorporating vector velocity,

$$F_D = \frac{1}{2}C_D\rho A|\vec{v}|^2. \tag{3.2}$$

[1]The term "pass" refers to one orbit or, in the case of hyperbolic trajectories, the spacecraft encounter with the target body.

The drag coefficient is assumed to be $C_D = 2.2$, as is standard for theoretical satellites [22]. The density is more complex to model as it depends on altitude and the specific planet or moon. For Earth, atmospheric density is well documented and published in the Earth Global Reference Atmospheric Model (GRAM) [23]. Atmospheric data varies in reliability for other bodies in the solar system. Similar models based on best available data have been developed for use in aerocapture mission design [24]. Where possible, atmospheric density is modeled using these GRAMs. Otherwise, density may be approximated using the exponential model [25]

$$\rho(h) = \rho_0 \exp\left(\frac{h_0 - h}{H}\right) \tag{3.3}$$

where h is altitude, H is the atmospheric scale height, and ρ_0 is a reference density corresponding to reference altitude h_0. Since we are using a pointmass gravity model, altitude can be computed simply as

$$h = |\vec{r}| - R_0 \tag{3.4}$$

where R_0 is the planet radius.

3.2 Model Benchmarking

A model incorporating the equations of Section 3.1 was developed in Mathematica. In order to test validity of the simulations, a nominal aerocapture trajectory must be compared between this model and an existing orbit code. NASA Copernicus Trajectory Design and Optimization System [26] is an orbit propagator developed at Johnson Space Center that is used for mission analysis. While not traditionally used to plan aeroassist maneuvers, it is a powerful and ubiquitous program that can serve well as a baseline against which to compare simulations. However, the need for a custom code arises from the limitations of Copernicus; specifically, its atmospheric drag model allows very little modification. It requires that drag area remain constant throughout maneuvers, which is not strictly accurate for magnetoshells. Additionally, it does not allow empirical atmospheric data for non-Earth bodies, instead requiring exponential approximations in the form of Equation (3.3).

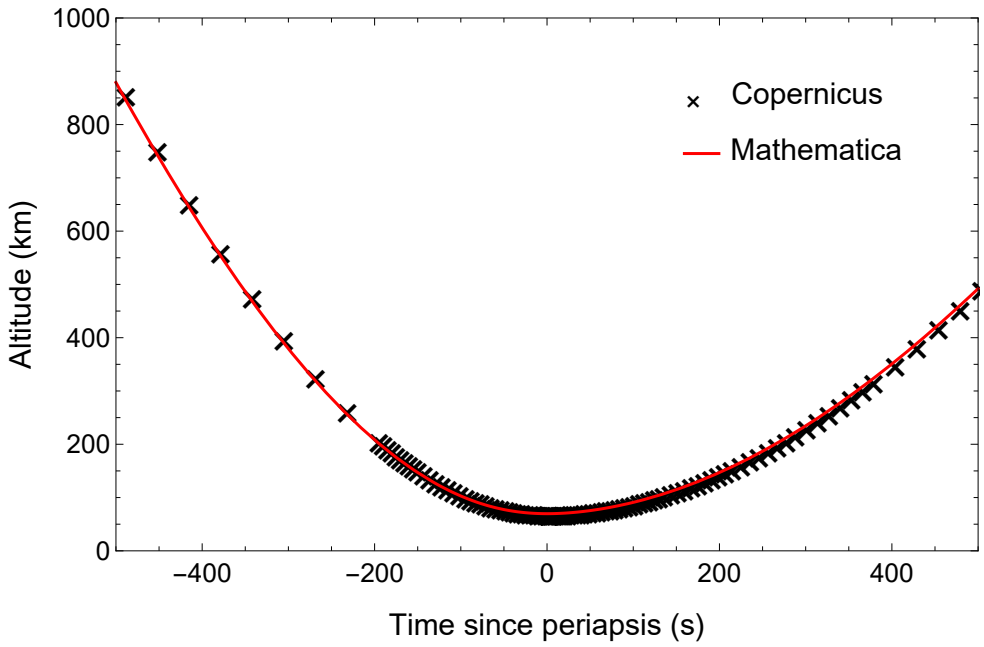

Figure 3.1: Comparison of simulations of a Martian aerocapture maneuver with Copernicus and a custom Mathematica code.

Benchmarking entails configuring the Mathematica code to run under the same restricted conditions as Copernicus and comparing trajectory results. This ensures that the orbit propagation model of Section 3.1 is reliable for known satellite physics. Once validated, individual components of the Mathematica code may be modified to develop a more physically faithful model in a controlled manner.

The code benchmarking is conducted for a maneuver using MAC to deliver a 60 ton payload to Martian orbit with a 720 m^2 magnetoshell. Mars' atmospheric density is modelled as Equation (3.3) with a scale height $H = 11.1$ km and $\rho_0 = 0.016$ kg/m^3 at reference altitude $h_0 = 0$ km [27]. Spacecraft drag is modelled as Equation (3.2) with a static area. Figure 3.1 shows the spacecraft altitude for both the Copernicus and Mathematica trajectory

results. It is clear that the Mathematica code satisfactorily reproduces the results obtained by Copernicus.

3.3 Continuously-Variable Drag

The Mathematica orbit model is now modified to calculate drag using a continuously-variable (CV) area. To do so, the static area A in Equation (3.2) is replaced with the magnetoshell effective area A_e in Equation (2.7):

$$A_e = \pi R_e^2 = \frac{\pi R_m^3}{r_{i,0}} = \frac{\pi q B_0}{m_i v} R_m^3. \tag{3.5}$$

Note that $A_e = A_e(v)$ is a function of spacecraft velocity. This is because the trapped ion contributing to drag maintains its pre-charge-exchange velocity in its Larmor orbit.

Recall that the constraints on the charge exchange mean free path λ_{cx}, Equations (2.9) and (2.10), correspond to a range of atmospheric density ρ in which MAC is operational. This effect must also be incorporated in the CV drag model. The constraints are rewritten here in terms of ρ so that they are compatible with the planetary density data. The upper bound of ρ is dictated by the smallest Larmor orbit in the magnetoshell, $r_{i,0}$, because once $\lambda_{cx} < \pi r_{i,0}$ then Equation (2.9) cannot be satisfied anywhere. The lower bound of ρ corresponds to L_0 as indicated by Equation (2.10). Combining these constraints, the range of operational density is

$$\rho_{min} = \frac{m_n}{L_0 \sigma_{cx}} < \rho < \frac{m_n}{\pi r_{i,0} \sigma_{cx}} = \rho_{max} \tag{3.6}$$

where $m_n = \rho / n_n$ is the atmospheric neutral particle mass. Note that $\rho_{max} = \rho_{max}(v)$ is a function of spacecraft velocity through $r_{i,0}(v)$; specifically, higher velocity limits ρ_{max} to smaller values.

Armed with Equations (3.5) and (3.6), the drag force in the equation of motion can be modified to capture CV effects. The drag force is now

$$F_D(\rho, \vec{v}) = \begin{cases} \frac{1}{2} C_D \rho A_e(v) |\vec{v}|^2, & \rho \in [\rho_{min}, \rho_{max}] \\ 0, & \rho \notin [\rho_{min}, \rho_{max}] \, . \end{cases} \tag{3.7}$$

By using this drag model in the equation of motion, the magnetoshell physics described by Kirtley's model (Section 2.2) are appropriately captured in real-time along the flight path. This allows modellers to step away from some of the limitations imposed by Copernicus and use the Mathematica model as a trajectory design and analysis tool.

3.4 Mission Simulations

The Mathematica code is used to reproduce two mission simulations from Kirtley [14]. They are a 60 ton cargo delivery to Mars and a 1 ton orbiter delivery to Neptune. In both cases, initial satellite conditions are generated by designing an appropriate approach trajectory in Copernicus and outputting $\vec{r}$ and $\vec{v}$ at some time before atmospheric entry. The orbits are then propagated in the CV Mathematica orbit model starting from these initial positions and velocities.

3.4.1 Assumptions

The atmospheric density at Mars is interpolated from values obtained in the Mars-GRAM [28]. The atmosphere is assumed to be made up of mostly CO_2 with a particle mass of $m_n = 44$ amu. Following Kirtley, the magnet radius is $R_m = 2.5$ m and the field strength set to $B_0 = 370$ G. Neptune's atmosphere is modeled as Equation (3.3) with a scale height of $H = 19.7$ km and reference density $\rho_0 = 0.45$ kg/m^3 [29]. A molecular hydrogen and helium atmosphere is assumed with a particle mass of $m_n = 3$ amu. The magnet radius is $R_m = 1$ m and field strength is $B_0 = 326$ G. These assumptions are summarized in Table 3.1.

3.4.2 Discussion

Several plots summarizing the simulations are found in Figure 3.2. For MAC at Neptune, the magnetoshell inflates to around 14 meters in diameter ($A_e \approx 160$ m^2) for a pass with a minimum altitude of 282 km. At Mars, the diameter is around 30 meters ($A_e \approx 700$ m^2) with a minimum altitude of 70 km. In both cases, the CV nature of the magnetoshell is evident.

Parameter	Neptune	Mars	Unit
Atm. species	H_2, He	CO_2	
Atm. model	Eq. (3.3)	GRAM	
m_n	3	44	amu
R_m	1	2.5	m
B_0	326	370	G
R_e	7–7.5	14.4–15.7	m
Peak drag F_D	27	465	kN
Peak dyn. pres. Q	77	310	Pa
Min. altitude h	282	70	km

Table 3.1: Assumptions (top half) and some key results (bottom half) for Neptune and Mars mission simulations using MAC.

The area increases as the spacecraft loses velocity through the atmosphere. The effect is more pronounced at Mars where the Δv is a larger percentage of orbit velocity. In both cases the magnetic field B_0 is maintained at a constant value; the area could be modulated even more drastically by controlling input to the magnet.

One feature prominent in Figure 3.2 is that the duration over which drag is produced is actually a short window. This indicates that the magnetoshell should remain deactivated until just before it can effectively generate drag in order to reduce the large energy storage requirements on the satellite. Future mission designs utilizing MAC must take advantage of this fact. The peak drag experienced by the craft (see Table 3.1) corresponds to accelerations of just 2.75 g for Neptune and 0.8 g for Mars, which are more than manageable from a spacecraft design standpoint. Perhaps more important is the very low maximum dynamic pressures observed. Typical expected dynamic pressures for Martian and Neptunian aerocapture missions are around 10–20 kPa [30, 31]. This simulation shows MAC able to operate at altitudes where peak dynamic pressure is 2–3 orders of magnitude lower.

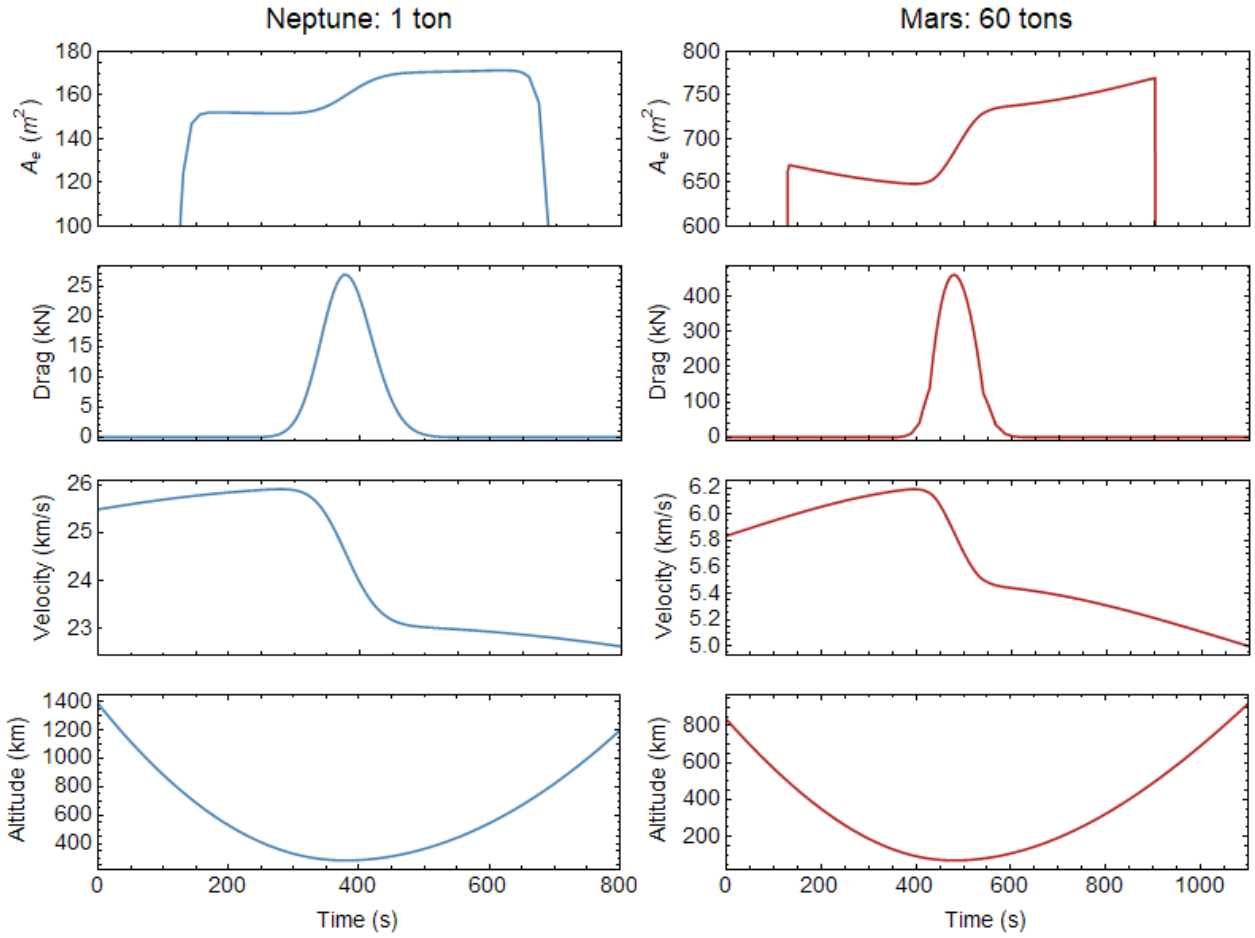

Figure 3.2: MAC for a 1 ton Neptune payload (left) and 60 ton Mars payload (right).

3.5 Discussion

The use of this code for the two simulations proves the feasibility of a self-consistent orbit propagator that computes magnetoshell parameters and applies them to the equations of motion. Improving the fidelity of simulations is a matter of upgrading modules within this framework rather than reinventing it. Furthermore, it opens up the possibility of incorporating a dynamic magnetoshell calculator into an even higher fidelity orbit propagator for broad use in aeroassist mission analyses.

It must be noted that this model is imperfect. Its aim was to apply the Kirtley model

to compute magnetoshell area dynamically along the trajectory of an aerocapture pass. In this, it has succeeded. However, further improvements may be made to abstract it from the simplistic scaling of the Kirtley model. For instance, the drag may not behave as in the form of Equation (3.2) since there is no discrete boundary of the plasma. Instead, the rate of neutral particle capture as a function of the radial plasma density may be measured to find a true drag force on the magnetoshell. Such improvements to the understanding of magnetoshell drag will be the result of plasma modelling beyond the scope of this thesis. Furthermore, the effects of lift and drag on the spacecraft body itself have not been considered; this analysis has thus far assumed such forces are negligible compared to the parachute effect of the plasma. However, a model incorporating full vehicle equations of motion (such as [32]) could support or disprove this claim.

It is due to these limiting approximations that the magnetoshell must be tested in an orbit-representative environment. The fidelity of the orbit code hinges on the physical accuracy of the magnetoshell drag computation. This must be achieved either by characterizing MAC in-flight or by developing a ground test whose results are folded into a computational model. The next two chapters focus on research avenues that can enhance the understanding of magnetoshell drag in operational regimes.

Chapter 4
CUBESAT DEMONSTRATION MISSION

As discussed in Section 1.3, a flight demonstration of MAC is an attractive option for proving feasibility of the concept due to the difficulty of ground testing in a representative environment. With this in mind, a CubeSat is designed at the system level whose mission is to demonstrate successful deployment of a magnetoshell in an orbital environment. Though the work detailed here is specific to one potential mission on a small spacecraft, the design principles and parameters used are applicable to developing any magnetoshell subsytem aboard a satellite of any scale.

4.1 System Design

4.1.1 Parameter Space

As a starting point for the system design, the parameters that impact mission efficacy are identified. Given the limitations on CubeSat orbits, the mission will not be able to demonstrate a hyperbolic-to-elliptic orbit insertion. Instead, consider the effectiveness of the magnetoshell in terms of the total impulse it can impart to the spacecraft. Let $I_M - I_0$ be the impulse gained over a time Δt_M when the magnetoshell is activated (where I_0 is the nominal impulse of atmospheric drag on the spacecraft body during the same time). Then the impulse gained by activating the magnetoshell for Δt_M during a certain period $\Delta t_{tot} \geq \Delta t_M$ is

$$f_I = \frac{I_M - I_0}{I_{tot}} \approx \frac{\Delta t_M}{\Delta t_{tot}} \left(\frac{F_M}{F_0} - 1 \right) \tag{4.1}$$

where F_M and F_0 are the magnetoshell and spacecraft-only drag forces, respectively, and the impulse is approximated as $I_* \approx F_* \Delta t_*$. f_I is an indicator of how effective the magnetoshell is at slowing the spacecraft compared to pure kinetic drag. $f_I = 0$ means that the magnetoshell

provided no change to the spacecraft's orbit; therefore f_I should be maximized in system design.

The ratio of magnetoshell drag to nominal drag can be written as

$$\frac{F_M}{F_0} = \frac{\frac{1}{2}C_D\rho A_e v^2}{\frac{1}{2}C_D\rho A_0 v^2} = \frac{A_e}{A_0} \tag{4.2}$$

where A_0 is the drag area of the satellite alone. Expanding this relation with the details of A_e from Equation (3.5), it becomes

$$\frac{F_M}{F_0} = \frac{\pi q B_0 R_m^3}{m_i v A_0} \tag{4.3}$$

Furthermore, the magnetic field strength B_0 can be approximated for a coil as

$$B_0 \sim \frac{\mu_0 I}{R_m} \tag{4.4}$$

where I is the sum of current in the electromagnet. Substituting this definition into the drag ratio, the final term is

$$\frac{F_M}{F_0} = \frac{\pi \mu_0 q I R_m^2}{2 m_i v A_0}. \tag{4.5}$$

The magnetoshell activation time Δt_M is limited by engineering constraints on the magnet. Applying the current needed to produce a magnetic field will dissipate Ohmic power in the form of heat. This poses a problem to the spacecraft since heat cannot be easily transferred away from the magnet in space. Suppose the magnet must not exceed a certain temperature increase ΔT_{max}. The relationship between the power P supplied to the magnet and this temperature change is

$$P \approx \frac{m_c c_p \Delta T_{max}}{\Delta t_M} \tag{4.6}$$

where m_c is the mass of the magnet coil and c_p is the specific heat of the coil material. This relationship gives a constraint on the magnetoshell activation time,

$$\Delta t_M = \frac{m_c c_p \Delta T_{max}}{P} \tag{4.7}$$

Substituting Equations (4.5) and (4.7) into Equation (4.1), an expression is obtained for f_I in terms of spacecraft design parameters:

$$f_I = \frac{m_c c_p \Delta T_{max}}{P \Delta t_{tot}} \left(\frac{\pi \mu_0 q I R_m^2}{2 m_i v A_0} - 1 \right). \tag{4.8}$$

Many of these variables are somewhat fixed. For instance, particle properties m_i and q are largely dictated by the atmospheric species. The nominal time Δt_{tot} is a scale time dictated by the character of the orbital pass; even with tweaks to the trajectory, it remains a similar order of magnitude. The same argument applies to orbit velocity v. Copper will be used for the magnet due its favorable conductivity and thermal properties, setting c_p and ΔT_{max}. A_0 is a function of spacecraft geometry which is effectively fixed for a CubeSat. This leaves a few variables to control, which are the critical design parameters: m_c, P, I, and R_m. Notice that all four parameters revolve around magnet design–m_c and R_m the geometry, P and I the electrical characteristics. Because of this, the system design is largely a matter of designing a magnet within the confines of the satellite bus.

Equation (4.8) implies several things about the system design. For instance, it is clear that maximizing magnet radius R_m has a strong impact on magnetoshell effectiveness. Similarly, a heavier magnet is able to absorb more heat and therefore remain activated longer. Both of these effects are limited by the maximum mass and spatial constraints of the satellite itself. There is an interesting relationship between P and I; increasing current to the magnet has a positive effect on impulse, but since $P \propto I^2$ the net effect is detrimental. Therefore, current must be maximized for a constant power output, implying the coil resistance should be kept to a minimum. This drives the magnet design toward many parallel wire arrangements instead of one long wound coil.

4.1.2 Tradeoffs and Considerations

Armed with the parameters of interest for MAC satellite design, the limiting considerations and tradeoffs between certain factors must be identified. Crucial to a flight demonstration mission is that its results are definitive and observable; the change in flight path caused by activation of the magnetoshell must be measured. For an object as small as a CubeSat, radar tracking may prove tricky and resource-intensive. Additionally, the change in velocity or orbital period may be very small and observation windows would make it difficult to compare measurements directly before and after magnetoshell activation. The

CubeSat is, however, expected to follow a predictable pattern of orbital decay. Activating the magnetoshell at perigee will cause a sharp drop in apogee altitude during the same orbit period.[1] Comparison of the post-activation apogee with the altitude expected from standard orbit decay provides a metric of successful magnetoshell drag. Measuring this altitude change Δh_a is straightforward as onboard GPS is a standard CubeSat sensor. The mission should therefore be designed to achieve maximum altitude change per activation in order to definitively prove magnetoshell feasibility.

Another important aspect of a flight demonstration is that the system resembles a potential future application of MAC. In practice, this means the magnetoshell size R_e should be substantially larger than the spacecraft to accurately portray an aerocapture-style configuration. However, generating a larger magnetoshell requires higher power P to strengthen B_0. Due to the hard limit on stored energy aboard the CubeSat, this higher power shortens the time of activation Δt_M. This reduction lowers the impulse fraction f_I and therefore Δh_a. All of this implies a tradeoff between the realism of the demonstration (as defined by R_e) and the measurability of success (as defined by Δh_a). The final design must address the balance of these factors.

Designing the orbit of the CubeSat also introduces an interesting tradeoff. The mission must be relatively low-altitude to achieve the desired high density operation. However, lower altitudes cause orbit decay due to the increased nominal atmospheric drag, eventually leading to deorbit. The mission must be long enough to repeatably demonstrate successful magnetoshell drag, but at low enough altitudes that the density is representative of a real maneuver. This also limits the number of times the magnetoshell may be activated during the mission. Each activation is very energy-intensive, and the CubeSat must recharge the magnet power source, which could take hours or days. At very low altitudes, the recharge time could even be close the the whole mission lifetime. Thus it becomes necessary to sacrifice high density in favor of extending the mission life.

---

[1] Perigee and apogee refer to the lowest- and highest-altitude points, respectively, in a spacecraft's orbit around Earth.

4.2 CubeSat Mission

The CubeSat bus was selected because it is an inexpensive and well-proven testbed for novel technologies at the university level. However, it carries some limitations. First, supposing a 3U size (10×10×30 cm), the mass cannot exceed 4 kg [33], a stringent requirement when magnet design is involved. Furthermore, nearly all CubeSats are launched as secondary payloads with little to no control over their final orbit [34]. Thus this demonstration mission will not truly be "aerocapture" since a hyperbolic trajectory is out of the question. However, this does not hinder the usefulness of the demonstration; for example, NASA does not require large-scale flight testing at Earth in order to prove feasibility for aerocapture at Mars [35], meaning a CubeSat demonstration is sufficient.

4.2.1 Parameter Selection

Several parameters were set first based based on the geometric and mass constraints of the CubeSat. A 3U bus was selected to accomodate enough room for the bulky power system needed by the magnet. The magnet radius should be maximized according to Equation (4.8); it was limited to $R_m = 35$ cm, as this was the largest reasonable radius a stowed magnet could be deployed to from a 3U package. ΔT_{max} was deemed 300 °C for the magnet due to standard copper wire insulation. The coil mass was set at $m_c = 1.5$ kg semi-arbitrarily to fit with standard CubeSat components within the 4 kg mass budget. The highest possible altitude is ∼400 km since the most likely flight opportunities for a CubeSat are secondary payloads en-route to the International Space Station.

With these parameters decided, several potential orbits were simulated in Copernicus to determine an appropriate perigee altitude. Various dimensions were tested, with perigees ranging from 150 km to 400 km and mission lifetimes from 3 days to 3 months. 220 km was ultimately chosen because it yielded a nominal mission life of 21 days, enough to test the magnetoshell five times, and had a suitable atmospheric density for generating plasma drag.

Based on spatial constraints in the CubeSat and off-the-shelf spacecraft batteries, maxi-

Parameter	Value	Unit
Magnet radius R_m	35	cm
Magnetoshell radius R_e	60	cm
Magnet mass m_c	1.5	kg
Batteries voltage	42	V
Batteries current	5.4	A
Batteries power P	226	W
Burn time Δt_M	800	s

Table 4.1: CubeSat system-level design parameters.

Braking duration (s)	MAC Area (m^2)	Δv (m/s)	Δh_a (km)
60	4.1	5.8	12.3
400	1.6	13.7	26.5
800	**1.1**	**15.8**	**31.1**
1200	0.9	14.9	30.8
1600	0.8	13.5	28.9
2400	0.6	10.8	24.8

Figure 4.1: Burn time optimization.

mum onboard energy is 96 W-hr (and is in fact limited to 100 W-hr by the CubeSat design specification [33]). This number was used to perform an optimization of burn time Δt_M as it relates to magnet power P and change in apogee Δh_a (see Figure 4.1). A burn time of $\Delta t_M = 800$ s provided the highest Δh_a. The final set of system-level parameters is given in Table 4.1.

4.2.2 Hardware and Flight Operations

Some prototype design was carried out based on the results of the system parameter selection. Figure 4.2 shows the notional hardware layout of the CubeSat. The coil is stowed as a spool for launch and is deployed by four spring-loaded booms released by a pin-pull

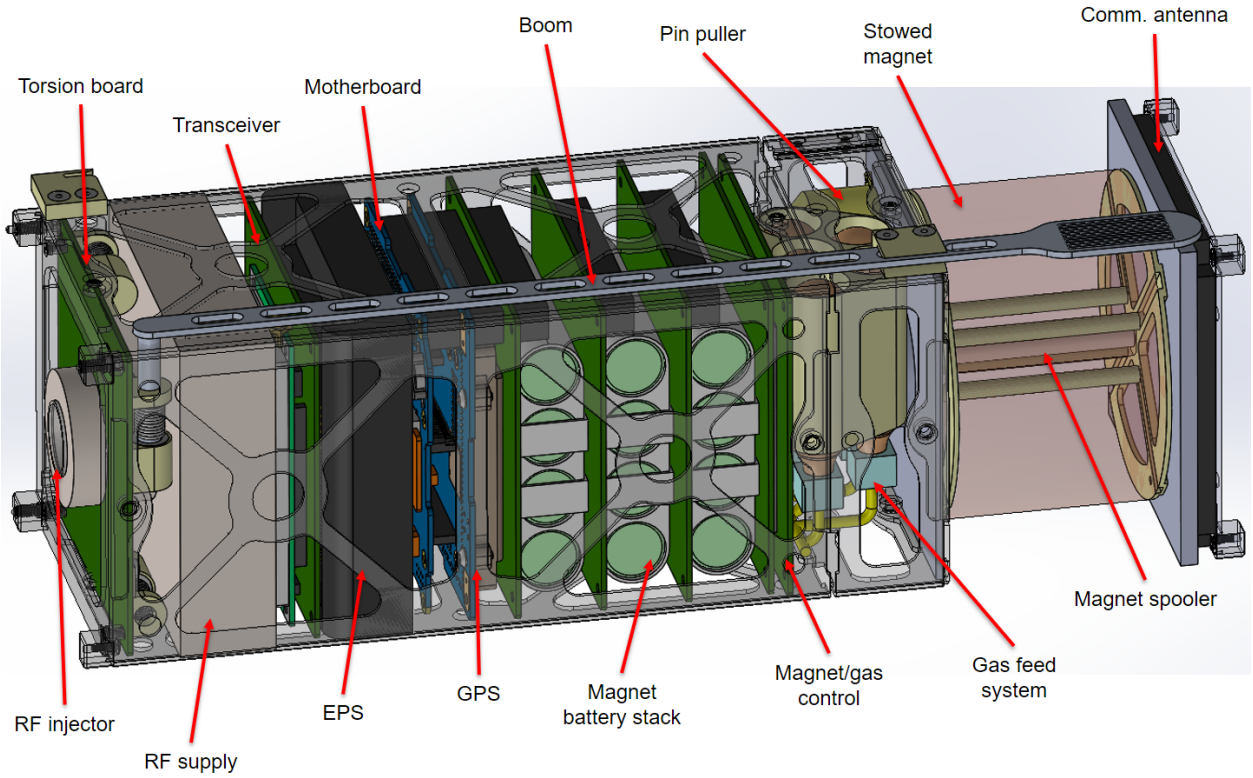

Figure 4.2: Internal CubeSat notional hardware.

mechanism. A plasma injection scheme consists of an RF plasma source at the center of the deployed magnet (the base of the CubeSat) and small pressurized Nitrogen tanks. Several standard commercial-off-the-shelf (COTS) components are included, such as a GPS sensor, communications transceiver and antenna, onboard computer, solar panels, and power distribution system. Figure 4.3 shows a mockup of the CubeSat in its stowed and deployed configurations.

An overview of the flight is shown in Figure 4.4. The magnet remains undeployed for the first seven days, allowing the craft to drift from any other CubeSats released simultaneously and for the orbit and onboard systems to be fully characterized. Once the magnet is deployed the orbit decays at a higher rate. The magnetoshell will be activated five times before finally deorbiting after 17.5 days, significantly shorter than the nominal decay time of 21 days. Each

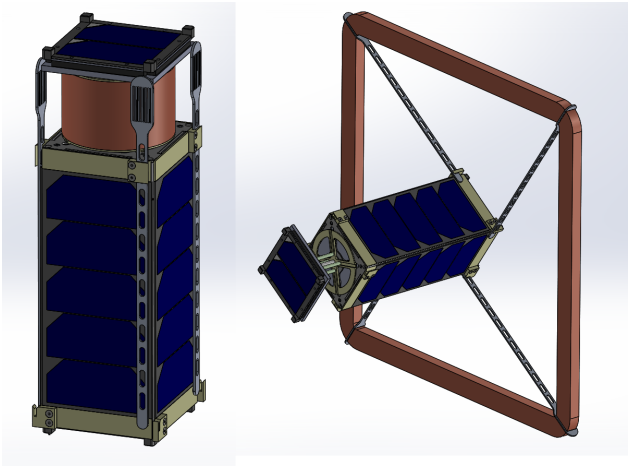

Figure 4.3: Magnet-stowed and magnet-deployed configurations of the CubeSat.

activation lowers the apogee by 10–34 km, easily detectable by the GPS sensor.

4.3 Discussion

The design process outlined here is a useful tool that may be applied to many missions of interest for MAC. However, several lessons were learned from the design of this specific flight demonstration. The primary drawback of this mission is the extreme size limitations imposed by the CubeSat bus. It was discovered early that a magnet fixed to the chassis would not be large enough to generate meaningful drag. Since $A_e \propto R_m^3$, maximizing the magnet radius is the most effective way to gain drag and thus drives the design toward a deployable coil. Efforts to prototype this deployment scheme were largely fruitless as the design complexity and coil rigidity proved impossible to keep mounted in the 3U form factor. Many CubeSats have used lightweight deployable booms, solar sails, and deorbiting skirts, yet none have ever deployed a system with the large mass and stiffness of the copper coil attempted here. Making this design feasible would require a breakthrough in CubeSat deployable technology beyond the scope of this thesis.

Yet another drawback is the power limit imposed both by the spatial constraints and the CubeSat specification. Even operating at 226 W (which is very high power by CubeSat

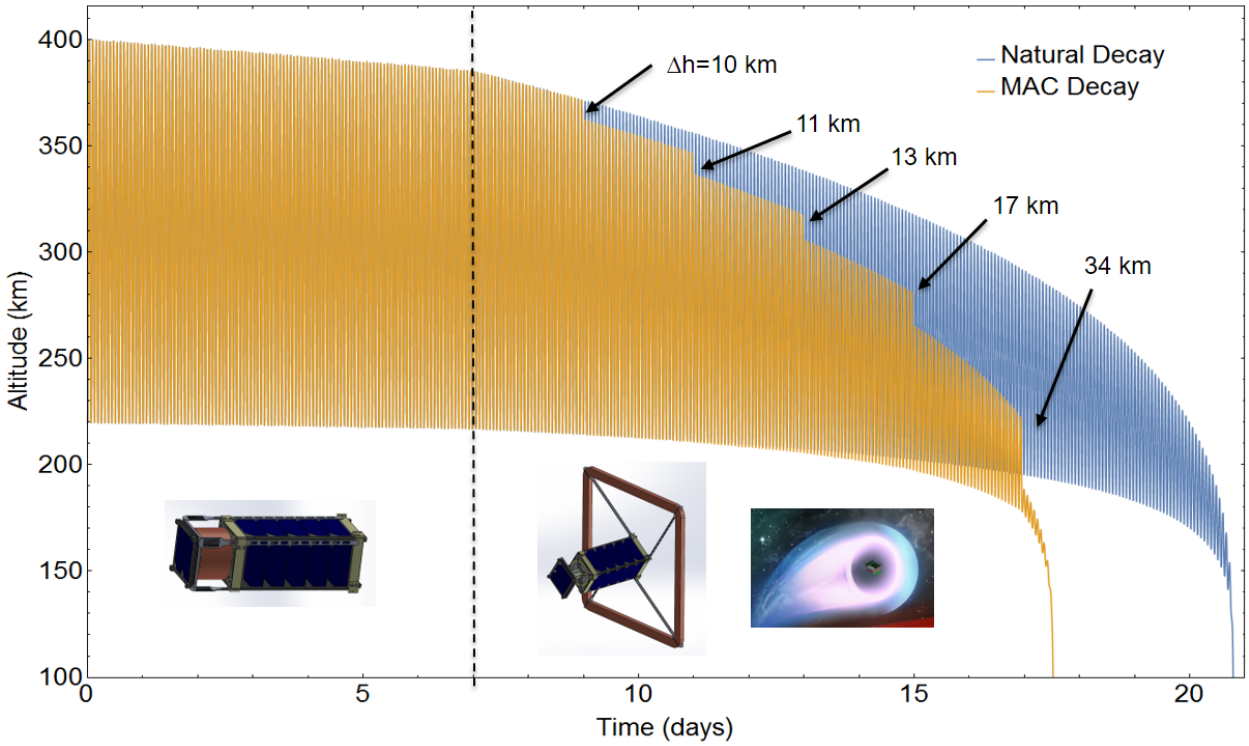

Figure 4.4: Mission profile for the MAC CubeSat. The magnetoshell is activated for 800 s every two days until deorbit.

standards), the effective magnetoshell size was scarcely larger than the coil itself. Not only does this imply a poor return on power for a MAC nanosatellite, it also means our scaling relations for system design break down at this size because the dipole magnetic field equations only apply in the far-field region $R_e \gg R_m$. Due to these challenges, it is likely that a demonstration mission of this configuration is intractable. However, given that these challenges are only introduced by the limitations of the CubeSat bus, a larger satellite could likely serve for a demonstration flight. Future attempts at flight demonstration could focus on the SmallSat class (∼100 kg) to relax the mass/spatial constraints while retaining the inexpensiveness of secondary payload development and launch.

Having determined that a flight demonstration of this caliber is unlikely, alternative approaches to proving concept feasibility must be examined. Although ground testing MAC

is currently not possible at relevant scales and regimes, experimentalists may be able to get around these limitations by developing subscale demnstrations. The following chapter gives an overview of what such an experiment may look like.

Chapter 5
SUBSCALE EXPERIMENT DESIGN

The challenges of producing a CubeSat mission to demonstrate MAC in an orbit environment necessitate some form of ground testing. As discussed earlier, testing a magnetoshell at full scale is practically impossible with current wind tunnel technology. However, it may be possible to develop a neutral beam capable of simulating atmospheric flow into a scale model magnetoshell. The goal of such an approach is to test MAC in a way that overcomes the burdens of a CubeSat flight while being more cost-effective than a larger satellite mission. Additionally, this approach facilitates rapid research and development of magnetoshell systems optimized for aerocapture maneuvers. While not as physically faithful as a flight demonstration, a carefully designed experiment may suffice to prove feasibility of MAC in the relevant regime.

5.1 Low-Energy Neutral Beams

Neutral-species beams have been a subject of research in materials processing for the past few decades due to their application in kinetic-energy-enhanced silicon etching [36]. Many techniques for extracting a neutral beam have been explored, but the focus here is on one which utilizes surface and volume neutralization of an accelerated plasma [37]. This technique can produce beams of the desired energy for application to MAC and is relatively simple to implement for a plasma-equipped lab. This technique is herein referred to as the ICP neutral beam because it is formed from an inductively-coupled plasma (ICP).

Figure 5.1 shows a schematic overview of an ICP neutral beam. A high-density plasma is generated between two electrodes forming an acceleration region. The anode, a positively-biased plate, causes an acceleration of ions across the sheath at the cathode, a grounded

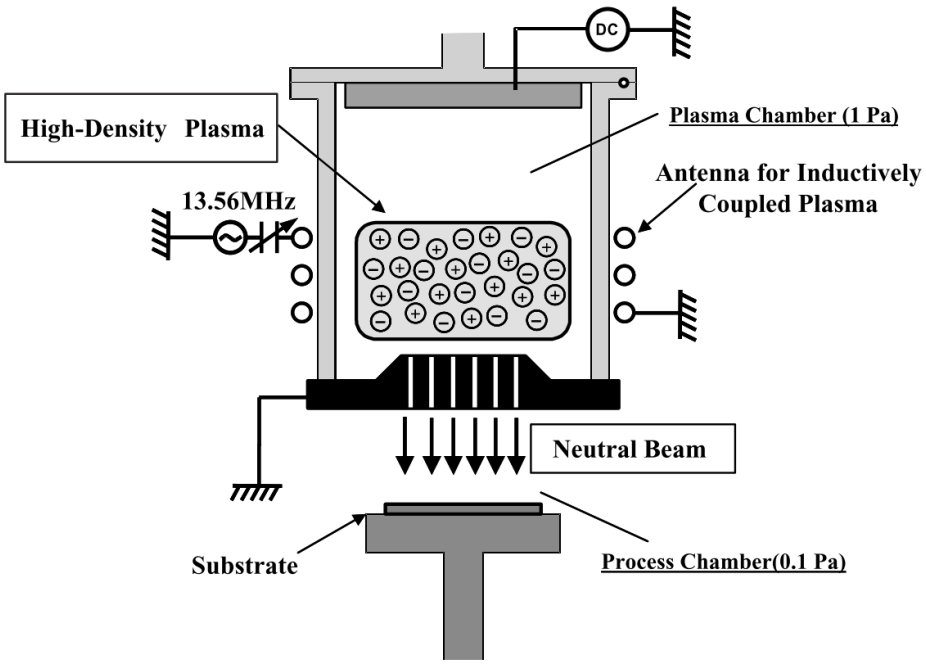

Figure 5.1: Diagram of an ICP neutral beam source using an ion extraction and neutralization grid [38].

"neutralization grid." The grid is a plate containing small (sub-mm) holes that neutralize ions as they pass through. These apertures have a relatively high aspect ratio (plate thickness over hole diameter). The neutralizing mechanism is a combination of charge exchange with background gas and glancing collisions with the grounded inner walls of the aperture. Since this plate is both a grid and an electrode, it acts to simultaneously extract and neutralize the ions for beam production.

Economou describes the importance of plasma "moulding" in the neutralizing effect of the grid [37]. Moulding refers to the shape of the plasma sheath around the openings in the grid (see Figure 5.2). It is desirable to have a sheath thickness L_{sh} on the order of the hole diameter D so that glancing collisions are maximized. This enhances both the neutralization efficiency and the beam directionality. Samukawa et al. found that the neutralization efficiency is increased with increasing aspect ratio [38]. They also found that a higher aspect

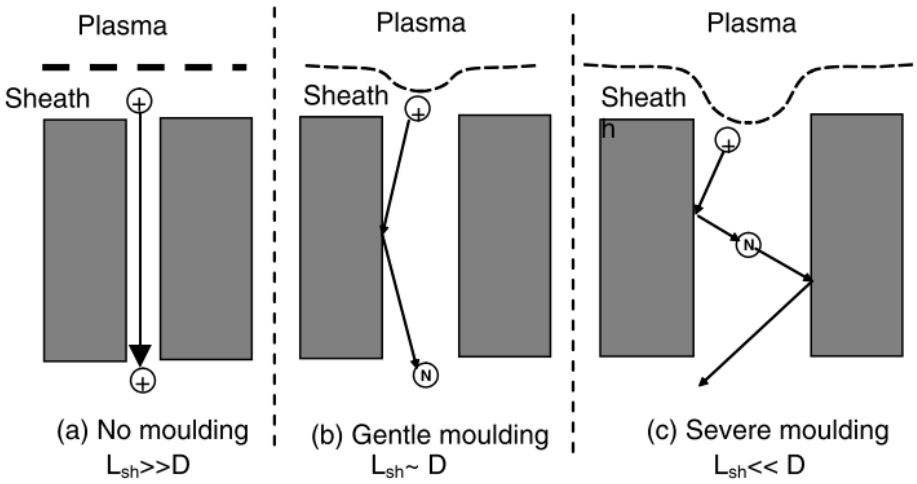

Figure 5.2: Effect of plasma moulding on the surface neutralization of ions [37].

ratio confines electrons in the acceleration region, extracting exclusively the neutral beam species.

The suitability of an ICP neutral beam to simulating atmospheric flow is not yet demonstrated. The chief concerns of this approach are beam energy, size, and density. Typical ICP neutral beam energies range from tens to thousands of eV while the atmospheric neutrals incident on the magnetoshell are below 10 eV. However, the range of experimental energies is only a consequence of the desired regime for silicon etching, nor is any physical limitation on energy proposed by past experimentalists. Neutral energies as low as 15 eV have been reported [39] which is of a similar magnitude to the orbit-entry regime. The beam size can presumably be made arbitrarily large by increasing the discharge chamber and grid diameter, though overwhelming plasma power requirements likely impose restrictions. Instead of expanding the beam, the magnetoshell is miniaturized and its interaction with the beam is observed through similarity parameters. Finally, the density of the beam should be sufficient to meet the requirements laid out by Equation (3.6). The neutral density n_n may be estimated from the equivalent current density j_{eq} reported in ICP neutral beam experiments.[1]

[1]The neutral beam flux is reported as an equivalent ion current density; that is, what the beam current

Using a higher-end reported value of $j_{eq} = 4$ mA/cm^2 [40] and a desired neutral velocity of $v = 7800$ m/s, the neutral density is

$$n_n = \frac{j_{eq}}{ev} = 3 \times 10^{16} \text{ m}^{-3} \tag{5.1}$$

which is about the density of Earth's atmosphere at 150∼200 km altitude. This indicates the neutral beam may be a reasonable approximation for orbital atmospheric flow, provided the ability to reproduce this current density at lower energies.

5.2 Experiment Design

This section discusses the considerations involved with designing a subscale MAC experiment using an ICP neutral beam. This will lay the groundwork for experimentalists who wish to ground test magnetoshells in orbit-entry regimes. A diagram of the layout of the neutral beam and subscale magnetoshell is shown in Figure 5.3. A flat-spiral antenna generates the ICP which is accelerated by parallel-plate electrodes and focused by a magnet into the neutralizing grid region. The neutral beam impacts the magnetoshell which is suspended or propped in the vacuum chamber away from the walls.

5.2.1 Similarity and Scaling

To apply subscale results to understanding MAC interaction with neutral atmosphere, similarity parameters must be identified that allow direct comparison across scales. One sensible parameter to use is the ratio of effective radius to magnet radius, R_e/R_m, since it captures information about the field strength, ion dynamics, orbital velocity, and magnet geometry simultaneously. This "trapping ratio" is nondimensional, making it useful for extrapolating observed results at one scale to any other. Combining Equations (2.7) and (4.4), the ratio is

$$\frac{R_e}{R_m} = \sqrt{\frac{\mu_0 I q}{m_i v}}. \tag{5.2}$$

---

density would be if the particles were ions rather than neutrals.

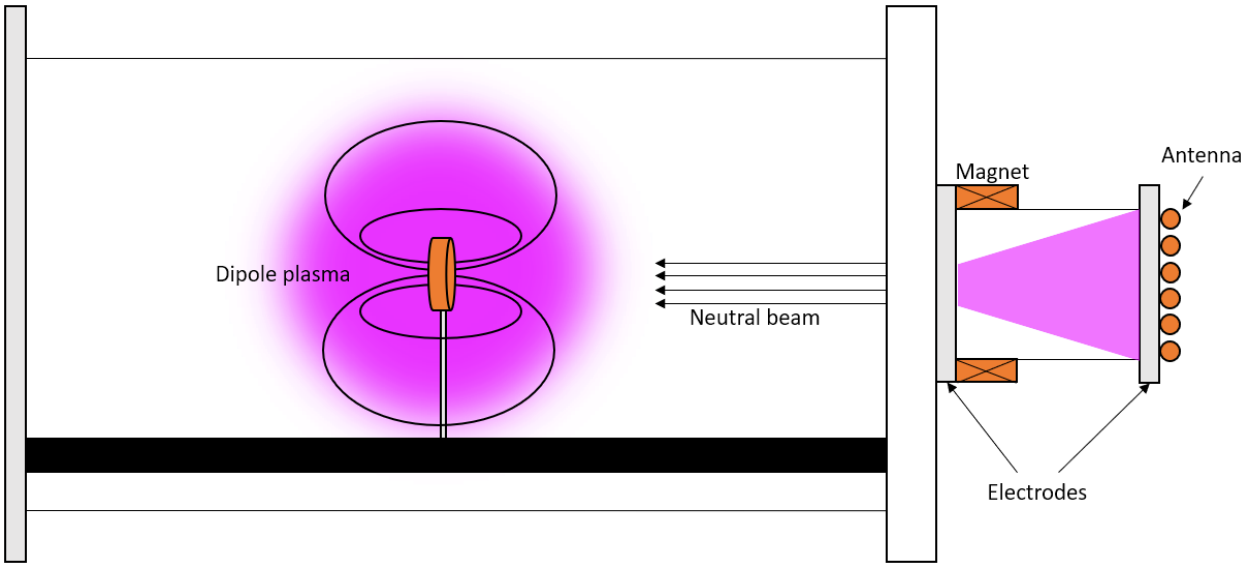

Figure 5.3: Possible layout for subscale magnetoshell ground test with ICP neutral beam.

In practice, since this ratio drives the requirements of the experimental hardware, R_e/R_m will be prescribed and the design tailored around it.

Equation (5.2) can be rearranged as

$$I = \frac{m_i v}{\mu_0 q} \left(\frac{R_e}{R_m} \right)^2 \tag{5.3}$$

for an expression describing the total current required in the magnet as a function of beam species, velocity, and trapping ratio. The current scales strongly with the trapping ratio, imposing a tradeoff whereby R_e/R_m must be sufficiently large but the current kept low. To achieve this, I will be limited by appropriate selection of beam species and energy. The current will also affect design of the magnet itself, as ohmic heating must be mitigated by its thermal mass.

5.2.2 Sample Design

Using this framework, a sample subscale experiment is developed and sized for a 30 cm-diameter cylindrical vacuum chamber as in the layout depicted by Figure 5.3. A trade study

Parameter	Value	Unit
Trapping ratio R_e/R_m	2.2	adim.
Magnet radius R_m	2.5	cm
Magnetoshell radius R_e	60	cm
Magnet mass m_c	0.28	kg
Turns N (26 ga.)	1220	#
Current I/N	6.5	A
Power	1.09	kW
Heating rate $\dot{T}$	10	°C/s
Beam species	N_2	n/a
Ion mass m_i	28	amu
Beam velocity v	7850	m/s
Beam energy T_n	6	eV
Bias voltage	9	V

Table 5.1: Design parameters for a potential subscale magnetoshell experiment. The top section details the magnetoshell while the bottom section details the ICP neutral beam.

found the final parameters which are detailed in Table 5.1. The first task is selecting a species and beam velocity. N_2 is chosen as the plasma and beam species for two reasons. First, it is the primary constituent of Earth's atmosphere and therefore simulates a flight demonstration. Second, charge exchange between nitrogen molecules is resonant and has a very large cross section, $\sigma_{cx} = 4 \times 10^{-19}$ m^2 [41], compared to lighter alternatives like helium. The beam velocity is set at 7850 m/s because σ_{cx} is at a near maximum and it is approximately the orbital velocity of a flight demonstration. Using these parameters, a trapping ratio of $R_e/R_m = 2.2$ is achieved with a 5 cm-diameter magnet. This demands a DC power of $P = 1$ kW which heats the magnet at a rate of $\dot{T} = 10$ °C/s. This heating rate is rather high, so the experiment must be operated in a quasi-pulsed mode, running only for

several seconds at a time.

5.3 Discussion

One advantage of the subscale experiment is the ability to characterize magnetoshell properties in an orbit-representative environment. Scientific investigation can be much more comprehensive than in a flight demonstration. For instance, a chief area needing to be addressed is the fuel and power requirement of seeding plasma to offset losses. Diffusion as a loss mechanism of the magnetoshell has not been characterized robustly. Previous models have assumed Bohm diffusion; the experiment can investigate whether this assumption is accurate in order to inform plasma sustainment needs. Diffusion may be characterized in a variety of ways. For example, a Langmuir probe sweep of temperature in a steady-state magnetoshell can be combined with magnetic field data to compute diffusion coefficients predicted by various models. These coefficients may then be compared with the observed injection rate required to maintain steady-state to determine which model most accurately describes diffusive losses.

Another property not well-understood is the structure of the charge-exchange region in the plasma. Interaction of reentry vehicles with the atmosphere is typically characterized by a bow shock which weakly ionizes the flow. However, the magnetoshell differs in that it does not have a solid body against which flow stagnates. Additionally, it is unclear whether this phenomenon would occur in these low density flows. This experiment offers an opportunity to image the magnetoshell interacting with the flow. The interaction may be observed with a filtered ICCD, for example, or even a high-speed camera (particle transits are on the timescale of micro-seconds). Knowledge of this interaction will help guide spacecraft configuration, plasma injection design, and perhaps even more complex magnet geometries to best utilize the ionization region of incoming particles.

By using a neutral beam flow source and a subscale magnetoshell, it may be possible to get around the current limitations on ground testing this device. The experiment described here offers a potential solution that enables rigorous investigation of magnetoshell physics in

an environment that accurately simulates aerocapture.

Chapter 6

CONCLUSION

This thesis has detailed some work advancing MAC closer to a state of proven feasibility. This low-TRL approach to orbit insertion requires proof-of-concept in an orbit-representative environment before it can be adopted by mission planners. Achieving this is no easy task given its unique size and operational regime.

One impediment to developing missions using MAC was the lack of a realistic orbit tool. Previous simulations had leveraged Copernicus which put restrictions on the accurate modelling of continuously-variable drag and atmospheric density. These issues are circumvented by developing a custom orbit propagator in which the spacecraft's state vectors and magnetoshell drag area are dynamically coupled. This code allows arbitrary density profiles so that MAC may be modelled at any atomspheric moon or planet. In its current state, magnetoshell physics are modelled according to the single-particle description provided by Kirtley[14]. However, any future analytic models may be easily integrated with the propagator to further enhance accuracy of drag calculations. This code enables investigation of optimal MAC maneuvers and informs us on phenomena that distinguish MAC from traditional aerocapture trajectories.

Though some of the technology behind MAC has been demonstrated in vacuum, full system feasibility has not yet been tested. It is thought that the most reliable way to achieve this is a flight demonstration mission. The goal is to launch MAC aboard a small, secondary payload satellite and use it to deorbit the craft over a series of activations, each measurable by a reduction of altitude. This would undoubtedly prove the concept, but faces implementation challenges due to the large energy and mass storage inherent to the dipole magnet. The satellite design process has been described by example of a 3U CubeSat with

a deployable coil. The CubeSat architecture ultimately fails to provide a good testbed for MAC. The onboard power simply cannot generate a large enough plasma and the difficulty of deploying a 1.5 kg coil demands major technology breakthroughs. For these reasons, alternative flight demonstration architectures should be examined, such as a larger satellite (100 kg-class) with a fixed-size magnet.

As an alternative approach to a flight demonstration, a potential experiment that could investigate MAC in an equivalent orbit regime has been described. This will be a subscale magnetoshell by necessity. However, through the similarity parameter R_e/R_m, all critical system parameters can still be manipulated (such as field strength, orbit velocity, and ion species) while maintaining fidelity to the full-scale magnetoshell. This approach is advantageous for the ability to investigate the device physics comprehensively and rapidly optimize magnetoshells. However, the neutral beam flow source proposed is unproven at the energies, sizes, and densities of interest for this experiment. A significant amount of effort would go toward adapting the ICP neutral beam technology for use as a MAC flow tool. Due to the lower risk and potentially lower cost associated with the subscale experimental approach, it is the recommended avenue for developing a proof-of-concept of MAC.

In all, these efforts bring MAC closer to realization as an orbit insertion technology. They help lay the groundwork for development of mission architectures through accurate trajectory modelling and system-level satellite design. Further, they open the door to experimentalists who may implement novel techniques for simulating high-altitude reentry flows and investigate magnetoshell physics. Expanding the body of work on MAC into these key areas will push it to a level on par with existing proposed aerocapture technologies.

BIBLIOGRAPHY

[1] Fernando Peralta and Steve Flanagan. Cassini Interplanetary Trajectory Design. *Control Engineering Practice*, 3(11):1603–1610, 1995.

[2] Jaime Esper. The Neptune/Triton Explorer Mission: A Concept Feasibility Study. Technical report, NASA Goddard Space Flight Center, Greenbelt, MD, 2003.

[3] Jeffery L. Hall, Muriel A. Noca, and Robert W. Bailey. Cost-Benefit Analysis of the Aerocapture Mission Set. *Journal of Spacecraft and Rockets*, 42(2):309–320, 2005.

[4] Juergen Mueller and Juergen Mueller. Thruster options for microspacecraft - A review and evaluation of existing hardware and emerging technologies. In *33rd AIAA/ASME/SAE/ASEE Joint Propulsion Conference and Exhibit*, Seattle, WA, 1997.

[5] Zachary R. Putnam and Robert D. Braun. Drag-Modulation Flight-Control System Options for Planetary Aerocapture. *Journal of Spacecraft and Rockets*, 51(1):139–150, jan 2014.

[6] Brett R Starr and Carlos H Westhelle. Aerocapture Performance Analysis of a Venus Exploration Mission. In *Atmospheric Flight Mechanics Conference and Exhibit*, 2005.

[7] David W Way, Richard W Powell, Karl T Edquist, James P Masciarelli, and Brett R Starr. Aerocapture Simulation and Performance for the Titan Explorer Mission. In *Joint Propulsion Conference and Exhibit*, 2003.

[8] W D Muth, C Hoffmann, and J E Lyne. Aerocapture for the TransHab/Ellipsled Vehicle Final Study Report for NASA Grant NAG1-2163. Technical report, 2000.

[9] Bret G. Drake, Stephen J. Hoffman, and David W. Beaty. Human Exploration of Mars, Design Reference Architecture 5.0. In *2010 IEEE Aerospace Conference*. IEEE, 2010.

[10] Stephen J. Hughes, F. McNeil Cheatwood, Anthony M. Calomino, Henry S. Wright, Mary Elizabeth Wusk, and Monica F. Hughes. Hypersonic Inflatable Aerodynamic Decelerator (HIAD)Technology Development Overview. Technical report, NASA Langley Research Center, San Jose, CA, 2013.

[11] Robert Dillman, John DiNonno, Richard Bodkin, Valerie Gsell, Nathanael Miller, Aaron Olds, and Walter Bruce. Flight Performance of the Inflatable Reentry Vehicle Experiment 3. In *10th International Planetary Probe Workshop*, San Jose, CA, 2013.

[12] Ethiraj Venkatapathy, Kenneth Hamm, Ian Fernandez, James Arnold, David Kinney, Bernard Laub, Alberto Makino, Mary McGuire, Keith Peterson, Dinesh Prabhu, David Empey, Ian Dupzyk, Loc Huynh, Prabhat Hajela, Peter Gage, Austin Howard, and Dana Andrews. Adaptive Deployable Entry and Placement Technology (ADEPT): A Feasibility Study for Human Missions to Mars. In *21st AIAA Aerodynamic Decelerator Systems Technology Conference and Seminar*, Dublin, Ireland, may 2011. American Institute of Aeronautics and Astronautics.

[13] Reuben R Rohrschneider and Robert D Braun. Survey of Ballute Technology for Aerocapture. *Journal of Spacecraft and Rockets*, 44(1):10–23, 2007.

[14] David Kirtley. A Plasma Aerocapture and Entry System for Manned Missions and Planetary Deep Space Orbiters. Technical report, 2014.

[15] R. M. Winglee, J. Slough, T. Ziemba, and A. Goodson. Mini-Magnetospheric Plasma Propulsion: Tapping the energy of the solar wind for spacecraft propulsion. *Journal of Geophysical Research: Space Physics*, 105(A9):21067–21077, 2000.

[16] John Slough. Plasma Sail Propulsion Based on the Plasma Magnet. In *30th International Electric Propulsion Conference*, Florence, Italy, 2007.

[17] Zachary R. Putnam, I. G. Clark, and R. D. Braun. Drag Modulation Flight Control for Aerocapture. In *2012 IEEE Aerospace Conference*, pages 1–10. IEEE, mar 2012.

[18] Carlos H Westhelle and James P Masciarelli. Assessment of Aerocapture Flight at Titan Using a Drag-Only Device. In *Atmospheric Flight Mechanics Conference and Exhibit*, 2003.

[19] J. Kesner and M. Mauel. Final report : Levitated Dipole Experiment. Technical report, Massachussetts Institute of Technology, Cambridge, MA, 2013.

[20] David Kirtley. ISS Launched CubeSat Demonstration of Variable-Drag Magnetoshell Aerocapture: Phase I Final Report. Technical report, 2014.

[21] Robert Bailey, Jeffrey Hall, Thomas Spilker, and Nora O'Kongo. Neptune Aerocapture Mission and Spacecraft Design Overview. In *Joint Propulsion Conference and Exhibit*, Reston, Virigina, jul 2004. American Institute of Aeronautics and Astronautics.

[22] Kenneth Moe. Density and Composition of the Lower Thermosphere. *Journal of Geophsyical Research*, 78(10):1633–1644, 1973.

[23] C. G. Justus, W.R. Jeffries III, S. P. Yung, and D. L. Johnson. The NASA/MSFC Global Reference Atmospheric Model-1995 Version (GRAM-95). Technical report, NASA Marshall Space Flight Center, Huntsville, AL, 1995.

[24] Aleta L. Duvall and C.G. Justus. Global Reference Atmospheric Model (GRAM) Series for Aeroassist Applications. In *43rd AIAA Aerospace Sciences Meeting and Exhibit*, 2005.

[25] David A. Vallado. *Fundamentals of Astrodynamics and Applications*. Microcosm Press, El Segundo, CA, 2001.

[26] Jacob Williams, Juan S. Senent, Cesar Ocampo, Ravi Mathur, and Elizabeth C. Davis. Overview and Software Architecture of the Copernicus Trajectory Design and Optimization System. In *4th International Conference on Astrodynamics Tools and Techniques*, Madrid, Spain, 2010.

[27] Dr. David R. Williams. Mars Fact Sheet, 2016.

[28] C. G. Justus and D. L. Johnson. Mars Global Reference Atmospheric Model 2001 Version (Mars-GRAM-2001) : Users Guide. Technical report, NASA Marshall Space Flight Center, Huntsville, AL, 2001.

[29] Dr. David R. Williams. Neptune Fact Sheet, 2016.

[30] Mary Kae Lockwood, Karl T Edquist, Brett R Starr, Brian R Hollis, Glenn A Hrinda, Robert W Bailey, Jeffery L Hall, Thomas R Spilker, Muriel A Noca, N O 'kongo, Robert J Haw, Carl G Justus, Aleta L Duvall, Vernon W Keller, James P Masciarelli, David A Hoffman, Jeremy R Rea, Carlos H Westhelle, Claude A Graves, Naruhisa Takashima, Kenneth Sutton, Joseph Olejniczak, Y K Chen, Michael J Wright, Bernard Laub, Dinesh Prabhu, R Eric Dyke, and Ramadas K Prabhu. Aerocapture Systems Analysis for a Neptune Mission. Technical report, NASA Langley Research Center, Hampton, VA, 2006.

[31] David M. Bose, Jeremy Shidner, Richard Winski, Carlie Zumwalt, F. M. Cheatwood, and Stephen J. Hughes. The Hypersonic Inflatable Aerodynamic Decelerator (HIAD) Mission Applications Study. In *AIAA Aerodynamic Decelerator Systems (ADS) Conference*, 2013.

[32] A Miele, T Wang, W Y Lee, and Z G Zhao. Optimal Trajectories for the Aeroassisted Flight Experiment. In *40th Congress of the International Astronautical Federation*, Malaga, Spain, 1989.

[33] CalPoly. Cubesat design specification, 2009.

[34] Thomas Zurbuchen. *Achieving Science With CubeSats: Thinking Inside the Box*. National Academies Press, Washington, DC, 2016.

[35] Randolph Lillard, Joe Olejniczak, Tara Polsgrove, Alice Dwyer Cianciolo, Michelle Munk, Charles Whetsel, and Bret Drake. Human Mars EDL Pathfinder Study: Assessment of Technology Development Gaps and Mitigations. In *IEEE Aerospace Conference*, 2017.

[36] Stephen R. Leone. Kinetic-Energy-Enhanced Neutral Etching. *Japanese Journal of Applied Physics*, 34:2073–2082, 1995.

[37] Demetre J. Economou. Fast (tens to hundreds of eV) neutral beams for materials processing. *Journal of Physics D: Applied Physics*, 41, 2008.

[38] Seiji Samukawa, Keisuke Sakamoto, and Katsunori Ichiki. High-Efficiency Neutral-Beam Generation by Combination of Inductively Coupled Plasma and Parallel Plate DC Bias. *Japanese Journal of Applied Physics*, 40:L779–L782, 2001.

[39] Seiji Samukawa, Keisuke Sakamoto, and Katsunori Ichiki. High-Efficiency Low Energy Neutral Beam Generation Using Negative Ions in Pulsed Plasma. *Japanese Journal of Applied Physics*, 40(Part 2, No. 10A):L997–L999, 2001.

[40] Seiji Samukawa, Keisuke Sakamoto, and Katsunori Ichiki. Generating high-efficiency neutral beams by using negative ions in an inductively coupled plasma source. *Journal of Vacuum Science & Technology A: Vacuum, Surfaces, and Films*, 20(5):1566–1573, 2002.

[41] Billy J. Nichols and Fred C. Witteborn. Measurements of resonant charge exchange cross sections in nitrogen and argon between 0.5 and 17 ev. Technical Report TN D-3265, NASA Ames Research Center, Moffet Field, CA, 1966.